Pure appl. geophys. 165 (2008) 1531–1554
0033–4553/08/081531–24
DOI 10.1007/s00024-004-0388-7



Pure and Applied Geophysics

# Time Evolution of Deformation Using Time Series of Differential Interferograms: Application to La Palma Island (Canary Islands)

Patricia A. Perlock,[1] Pablo J. González,[2] Kristy F. Tiampo,[1]
Gema Rodríguez-Velasco,[2] Sergey Samsonov,[1] and José Fernández[2]

*Abstract*—Differential interferometry is a very powerful tool for detecting changes in the Earth's crust where coherence conditions are good, but is difficult to employ in some volcanic areas due to dense vegetation. We apply two differential InSAR methods using the time series associated with the interferograms to perform a phase analysis on a data set for La Palma island (Canary Islands) from the ERS-1 and ERS-2 European Space Agency (ESA) satellites for the time period 1992 to 2000. Both methods involve choosing a master image from the database and creating a series of interferograms with respect to this image. The "Coherent Pixel Time Series" (CPTS) technique chooses pixels with good average coherence, aligns the unwrapped interferograms with a stable area and then performs an inversion to calculate the linear velocity to quantify the deformation. The Coherent Target Modeling (CTM) method calculates the temporal coherence of each pixel to identify stable targets and then determines the best velocity for each pixel by using a linear fit that maximizes the temporal coherence. Using these two methods we have been able to detect deformation on La Palma Island that has been previously undetectable by conventional InSAR methods. There is a roughly circular region on the Southern part of the island that is actively deforming at $\sim -4$ to $-8$ mm/yr. This region is located near the Teneguia valcano, the host of the last known eruption on La Palma in 1971. A thorough investigation of the possible sources for this deformation revealed that it was most likely created by a subsurface thermal source.

**Key words:** Time series, La Palma, InSAR, ground deformation modeling, differential interferograms, permanent scatterers.

## 1. Introduction

Measuring changes on the Earth's surface by means of Interferometric Synthetic Aperture Radar (InSAR) has become a popular research subject among the geophysical community. Differential InSAR involves calculating the difference in the phase between two images taken at different times by a spaceborne Synthetic Aperture Radar (SAR) and then correcting for geometry and topography. Use of this technique can be applied to large spatial areas where it is difficult to deploy land-based geodetic monitoring networks. It is particularly useful in monitoring natural phenomena such as landslides,

[1] Department of Earth Sciences, University of Western Ontario, London, Ontario, Canada.
[2] Instituto de Astronomía y Geodesia, CSIC-UCM, Madrid, Spain.

volcanoes and earthquakes but can be limited due to the repeat time associated with acquiring images.

Ground deformation and gravity changes are well known geodetic observables that can reflect the state of activity at a volcano, and for this reason a geodetic monitoring program should be implemented at almost every volcano around the world, but this is a very difficult objective to meet. New space-based geodetic techniques could produce a limited, prior knowledge of the background level of the ground deformation on a volcano using past recorded SAR images from the ERS satellites (ERS-1/ERS-2) launched by the European Space Agency. In the last decade, radar interferometry has become more than just a promising geodetic tool. This technique has proven to be useful in volcanic areas, capable of detecting displacements caused by shallow intrusions. Using large datasets of SAR images and statistical methods, interferometry techniques could detect slow long-standing inflation-deflation processes on deep magmatic reservoirs.

Using InSAR methods on volcanically active areas can be difficult because of steep slopes and dense vegetation due to their fertile soil. SAR images taken in mountainous regions that have steep slopes may have low coherence or lost information due to the geometric effects of phenomena such as foreshortening, layover and shadowing. Vegetation poses a problem because it changes quite rapidly in time. This causes the scattering properties to also change rapidly with time causing temporal decorrelation. One way of dealing with this problem is to implement the"Permanent Scatterers Technique"$^{TM}$ developed and patented by FERRETTI *et al.* (2000; 2001). This method involves finding a subset of pixels in the image that have their phase determined predominately by a stable point-like scatterer (PS). This reduces decorrelation because the degree of correlation in radar signals depends on the distribution of the scattering centers within a pixel. Therefore, analyzing only those pixels exhibiting correlation above a predefined threshold, should increase the chances of detecting deformation in a volcanic region.

The algorithm developed by FERRETTI *et al.* (2000; 2001) identifies PS pixels using the amplitude dispersions in a series of interferograms and uses temporal correlation in the phase analysis. This method tends to work best in areas where there is a high density of stable reflectors like man-made structures that will result in a large set of point scatterers. In natural terrains such as volcanic regions, this still poses a problem because there is a lack of natural point scatterers resulting in a small set of PS pixels and therefore, the results can be unreliable or misinterpreted. HOOPER *et al.* (2004) addressed this issue by modifying the algorithm to identify PS pixels based on phase analysis. The method chooses the initial set of PS pixels using a high amplitude dispersion threshold and then runs an iterative phase analysis on the pixels to determine a final set of PS pixels. Using temporal correlation in phase analysis is also not conducive to volcanic settings as volcanic deformation varies temporally. HOOPER *et al.* (2004) use spatial correlation in their phase analysis which allows the deformation to be calculated without making assumptions of its temporal history. By incorporating these two new aspects into the

algorithm HOOPER *et al*. (2004) were able to produce reliable deformation results in volcanic areas that were otherwise not detected.

The two methods presented here build upon the idea of using phase analysis to identify the deformation or linear velocity. Both approaches involve constructing a set of differential interferograms with respect to one master interferogram. The "Coherent Pixel Time Series" (CPTS) technique is based on the selection of pixels with good average coherence from the study period. Once these pixels are chosen, the unwrapped interferograms are "aligned" using a zero deformation zone, allowing for a complete reconstruction of the total deformation history for each pixel. The deformation history is then inverted to calculate the linear velocity and quantify the deformation. Finally, the linear model is adjusted by removing pixels with large RMS error or low average coherence. The Coherent Target Modeling (CTM) method uses the stability of the phase to identify coherent targets. It does this by evaluating the temporal coherence (a measure of how stable the scatterer is over time) of each pixel. The deformation is quantified by iteratively searching through a set of velocity and DEM errors to find the combination that produces a maximum temporal coherence. Using the two methods presented in this paper, we have been able to detect deformation on La Palma island, Canary Islands that has been previously undetectable by other InSAR methods.

## 2. *La Palma: Canary Islands Geological Settings*

The Canarian Archipelago, situated off the NW coast of the African continent, is formed by a group of seven major islands (Fig. 1A). Even after a century of study, its origins remain under discussion and several hypothesis are proposed, such as a hotspot or mantle plume (PÉREZ *et al*., 1994; CARRACEDO *et al*., 1998; DAÑOBEITIA and CANALES, 2000), a region of compressional block faulting (ARAÑA and ORTÍZ, 1991), a rupture propagating from the active Atlas Range (ANGUITA and HERNÁN, 1975) or a unifying model (ANGUITA and HERNÁN, 2000). The islands rest on a transitional crust that is overlain by a sedimentary cover with a maximum thickness of 10 km in the eastern zone and a minimum of 1 km in the western sector (BANDA *et al*., 1981). The island of La Palma is the emerged part of an oceanic edifice of predominantly basaltic composition with a submarine base lying over the North Atlantic abyssal plain ($\approx$ 4000-meter depth). La Palma is resting on oceanic lithosphere of Jurassic age ($\approx$155 Myr, the "M25-isochron"), has a subaerial exposure that extends approximately 708 km$^2$, and reaches an elevation of 2500 m above sea level. The island is geologically divided into two main units: the Basal Complex (BRAVO, 1964; FÚSTER *et al*., 1968) or Submarine Edifice (CARRACEDO *et al*., 2001) and the Subaerial Edifices. The subaerial edifices are composed of shield volcanoes in the north (Garafía, Taburiente, and Cumbre Nueva volcanoes) and Cumbre Vieja volcano located on the southern ridge (NAVARRO and COELLO, 1993; ANCOECHEA *et al*., 1994) (Fig. 1B).

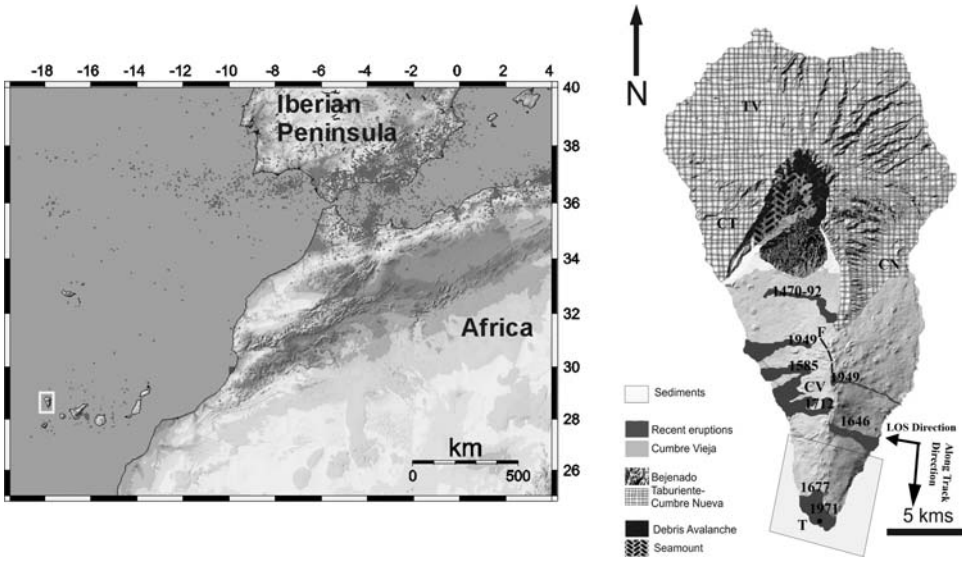


Figure 1

Figure 1A shows the geographical location of the Canary Islands and La Palma island (white rectangle) located off the NW coast of Africa. The grey dots represent seismicity at the region between 1973–2004 (Data source NEIC-USGS). Figure 1B is a geological map of La Palma redrawn after CARRACEDO *et al.* (2001) where TV = Taburiente Volcano; CT = Caldera de Taburiente; CN = Cumbre Nueva Volcano; F = Mapped Fracture at the summit of Cumbre Vieja (CV) volcano and T = Teneguia volcano. The area outlined in the south is the study area for our deformation, located near Teneguia volcano.

### *2.1. The Basal Complex: An Uplifted Seamount*

The Basal Complex outcrops at the base of the Caldera de Taburiente (a large depression located in the northern sector of the island). It consists of a succession of 1800 m of pillow lavas, hyaloclastic rocks and breccias of basaltic composition, crossed by trachytic and phonolitic domes and a large, dense network of basaltic dikes and gabbroic intrusion bodies (DE LA NUEZ, 1984). This unit is approximately 3–4 Myr old. The material appears to be hydrothermally altered with a low grade metasomatism, that has caused the recrystallization of minerals indicative of temperature conditions around 450–500°C and a pressure of 1–1.5 kbar (under 3000 m of lithostatic pressure). Eruptive activity in the caldera ceased 3 Myr ago at which point continuous uplifting and southwest tilting occurred and a strong erosional stage began, resulting in the deposition of breccias and debris avalanche deposits.

### *2.2. Subaerial Volcanism*

**Northern Sector**. Subaerial volcanism in the northern sector began approximately 1.7 Myr ago and ceased 0.4 Myr ago, creating several individual overlapping edifices

(CARRACEDO *et al.*, 2001; NAVARRO and COELLO, 1993). The first subaerial phase of the Northern Edifice (1.7–1.2 Myr) consisted of the Garafía volcano composed of basaltic lavas deposited unconformably over the submarine edifice. The Garafía volcano outcrops as erosive windows and its tabular formations are tilted 30°, concentrically centered on the submarine edifice (FERNÁNDEZ *et al.*, 2002). The volcano itself is approximately 400 m wide and rises approximately 2000 m above sea level. The second phase of development consists of the Taburiente volcano, which is separated from the Garafía volcano by an angular erosive unconformity suggesting that a large gravitational landslide must have destroyed the northern flank of the Garafía volcano (ANCOECHEA *et al.*, 1994; CARRACEDO *et al.*, 2001). The first phase was dominated by pyroclastic deposits which became progressively more lava-like. Subsequently, the emission centers were aligned in three rift zones (directed NW, NE and N-S) that extend concentrically out from the central part of the volcano which is approximately 3000 m in height.

The magmatic fertile zone migrated southwards along the N-S rift and a new high aspect ratio volcano known as the Cumbre Nueva Ridge formed, creating an instability in the northern sector. In the final building stage of this sector, Cumbre Nueva collapsed and generated a large landslide in the western flank around 0.56 Myr ago (NAVARRO and COELLO, 1993) leaving a depression that was quickly filled by lavas. The emission centers were limited to the interior of the depression creating the rapidly developed volcano, Bejenado (0.56–0.49 Myr) that is $\approx$600 m thick (CARRACEDO *et al.*, 2001).

**Southern Sector: Present Activity**. The southward migration of volcanic activity created a new and separate edifice in the south, the Cumbre Vieja volcano. The recent (upper Pleistocene-Holocene) volcanic activity in La Palma is concentrated in this volcano. Cumbre Vieja is formed by a succession of overlapping lavas and pyroclastic deposits from a large number of fissure eruptions that are oriented dominantly north-south. This volcano can be divided into two formations. The first is an older *cliff-forming* formation with basaltic and basanitic composition that is dated to be between 130–30 kyr. The second is a younger *scree-* and *platform-forming* formation created by strombolian activity with basaltic, basanitic and tephritic composition as well as sparse phonolitic domes that presently cover the Cumbre Vieja flanks (GUILLOU *et al.*, 1998; DAY *et al.*, 1999). Cumbre Vieja has been the most active volcano in the Canary Islands in historical and recent times, having had seven eruptions take place: Montaña Quemada (1470–1492), Tahuya (1585), Tigalate o San Martín (1646), San Antonio (1677), El Charco (1712), Nambroque or San Juan (1949) and Teneguía (1971) (ROMERO, 2000).

## *3. Data Processing and Time Series Analysis*

### *3.1. Previous Geodetic Monitoring*

La Palma island has not had a geodetic monitoring program in place to quantify the volcanic deformation until recently, and even now, only small steps have been

taken. Recently, Moss *et al.* (1999) have set up a geodetic network that has been used to produce three surveys using Electronic Distance Measuring (EDM) and Differential GPS (DGPS) techniques in the southern part of the island (between 1994–1997) and have detected displacements on the same order of magnitude as the associated errors. They argue that the western flank of the Cumbre Vieja volcano could potentially collapse in a megalandslide. At the same time, geological evidence of tectono-volcanic and purely volcanic ground movements on large time scales have recently been reported on the entire island (Hildenbrand *et al.*, 2003; Klügel *et al.*, 2005).

Campaign GPS missions that have been undertaken on La Palma have been unsuccessful in detecting the deformation found on Teneguia volcano because the area of deformation is very small and there are no GPS stations directly in this region. Classical interferometry that has been applied to detect deforming areas in the past (Massonnet and Sigmundsson, 2000; Fernández *et al.*, 2002) was not precise enough to detect the displacements thought to be present on Teneguia due to the dense vegetation in the area and the magnitude of the displacements. Here, two approaches are applied to obtain a complete history of the time-dependent evolution of the deformation from 1992 to 2000 on La Palma island.

### *3.2. Data*

We have studied an eight-year period, between 1992 and 2000, using the existing archive dataset from ESA SAR missions (ERS-1/ERS-2), to generate continuous high-resolution maps of the surface ground deformation on La Palma island, in order to evaluate the deformation in this volcanic area. To generate the interferograms, we have used 16 descending ERS-1 and ERS-2 SAR images (Table 1). After analysis of the precise orbit information and the time of acquisition, we have excluded the image from June 29, 1993 due to its large spatial perpendicular baseline.

### *3.3. Selection of Master Images*

One of the most important parts of the *Time Series Analysis of Interferograms* is the selection of the master image. It is necessary to have some independent parameters that can be used to determine that the master, chosen from the large dataset of SAR images, is reasonable. The Theoretical Cumulative Correlation (TCC) model is a simplified version of the model developed by Hooper (2006) that can be used to determine the best choice for a master image.

Suppose there are $N-1$ single-look interferograms formed with respect to one master from $N$ images. The master chosen to create these interferograms should be one that minimizes the decorrelation, and therefore maximizes the sum correlation of all the interferograms. The coherence can be modeled as the product of four terms: the temporal baseline ($T$), the spatial perpendicular baseline ($B_{\perp}$), the Doppler Centroid frequency

Table 1

*Available SAR images over La Palma, Canary islands. Track: 395, Frame: 3033. Incidence angle in the scene center is 23.2°, $B_\perp$ is the spatial perpendicular baseline between satellite acquisition in meters and $H_{amb}$, is the height of the ambiguity in meters. $LP_i$ stands for La Palma and the image number*

| Image | Date | Orbit | $B_\perp$ (m) | Time Span (days) | $H_{amb}$ (m) | Satellite |
|---|---|---|---|---|---|---|
| LP1 | 29/05/1992 | 4548 | − 130.4 | − 1178 | 72.4 | ERS-1 |
| LP2 | 07/08/1992 | 5550 | − 65.6 | − 1108 | 143.7 | ERS-1 |
| LP3 | 29/06/1993 | 5550 | − 451 | − 933 | 20.9 | ERS-1 |
| LP4 | 23/07/1993 | 10560 | − 37.7 | − 758 | − 250.4 | ERS-1 |
| LP5 | 01/10/1993 | 11562 | 12.7 | − 688 | − 745.8 | ERS-1 |
| LP6 | 11/06/1995 | 20423 | − 110.8 | − 70 | 85.2 | ERS-1 |
| LP7 | 20/08/1995 | 21425 | *Master* | *Master* | *Master* | ERS-1 |
| LP8 | 21/08/1995 | 1752 | − 101.9 | 1 | 92.6 | ERS-2 |
| LP9 | 24/09/1995 | 21926 | − 122.9 | 35 | 76.8 | ERS-1 |
| LP10 | 04/12/1995 | 3255 | − 191.1 | 106 | 49.4 | ERS-2 |
| LP11 | 08/01/1996 | 3756 | − 43.7 | 141 | 215.7 | ERS-2 |
| LP12 | 09/09/1996 | 7263 | − 303.3 | 386 | 31.1 | ERS-2 |
| LP13 | 14/10/1996 | 7764 | − 94.5 | 421 | 99.9 | ERS-2 |
| LP14 | 10/08/1998 | 17283 | 106.3 | 1086 | − 88.7 | ERS-2 |
| LP15 | 21/06/1999 | 21792 | − 110.7 | 1401 | 85.2 | ERS-2 |
| LP16 | 26/07/2000 | 26802 | 99.4 | 1751 | − 94.9 | ERS-2 |

(FDC) and the thermal noise (ZEBKER and VILLASENOR, 1992). A simple model for the total correlation is,

$$\rho_{\text{total}} = \rho_{\text{temporal}} \cdot \rho_{\text{spatial}} \cdot \rho_{\text{Doppler}} \cdot \rho_{\text{thermal}} \tag{1}$$

$$\rho_{\text{total}} = \left(1 - f\left(\frac{T}{T^c}\right)\right) \cdot \left(1 - f\left(\frac{B_\perp}{B_\perp^c}\right)\right) \cdot \left(1 - f\left(\frac{F_{DC}}{F_{DC}^c}\right)\right) \cdot \rho_{\text{thermal}} \tag{2}$$

where

$$f(x) = \begin{cases} x, & \text{for } x > 1 \\ 1 & \text{for } x < 1 \end{cases}$$

$\rho$ represents the coherence and the superscript $c$ denotes the critical parameter values. The critical parameter for a value is a threshold beyond which an interferogram will display almost complete decorrelation. These values are dependent on the dataset being used. Typical values for ERS data in arid regions are $T^c = 5$ years, $B_\perp^c = 1100$ m and $F_{DC}^c = 1380$ Hz (HOOPER, 2006). We have disregarded the Doppler Centroid frequency term for the following reason. The ERS-2 satellite was launched using three gyroscopes and functioned in this mode until the year 2000, at which time, a new one gyroscope mode was implemented. Since the year 2001, the satellite has been running in a zero-gyro mode. The Doppler Centroid frequency term included in Equation (2) is meant to account for the effect that the evolution of these gyroscope modes has had on the SAR Doppler Centroid frequency (MIRANDA *et al.*, 2004). Because we are dealing with images prior to the year 2001, we are able to neglect this term in our calculations. A master is chosen that

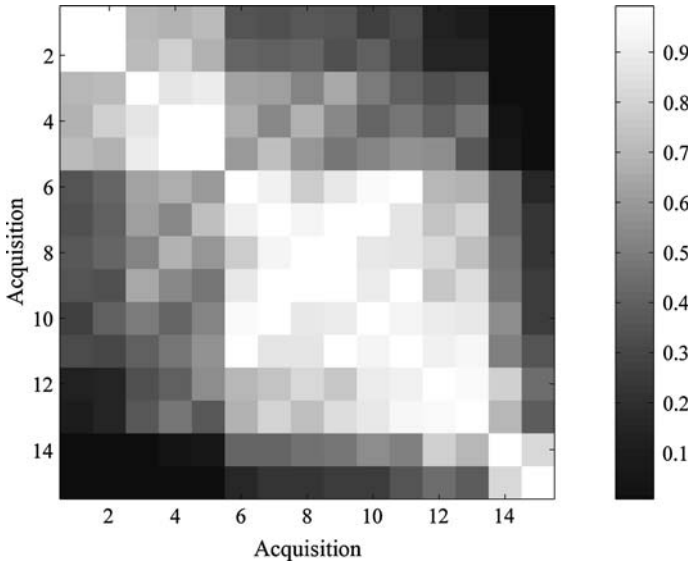


Figure 2
Theoretical coherence values for all combinations of individual interferograms using the Theoretical Cumulative Coherence model. The main diagonal containing high coherence values refers to the combination of interferograms with themselves and the highest values on this diagonal correspond with the master-master combination.

maximizes $\sum_{i=1}^{N-1} \rho_{\text{total}}$, assuming a constant value for $\rho_{\text{thermal}}$. Figure 2 shows the theoretical correlation values for each of the 15 interferograms using the TCC model. The main diagonal showing the highest theoretical correlation can be excluded as it is the master-master combination that cannot be used. Plotting the theoretical cumulative correlations for each master image (Fig. 3) shows that the images temporally centered in the database that have the highest theoretical correlations also have the highest theoretical cumulative correlations. These images are: image 6 = June 11, 1995; image 7 = August 20, 1995; image 9 = September 24, 1995; image 10 = December 4, 1995 and image 11 = January 8, 1996. From the TCC calculation, we have determined that the best images to use as master images are August 20, 1995 and December 4, 1995.

### *3.4. Preparation for Deformation Modeling*

The analysis begins by coregistering all of the slave images with one master to find an optimal transformation model that will transform the slave images into alignment with the master. The second step is to resample all of the interferograms into the same size by processing them all with the same region of interest (ROI). In this case, the original images are of the full island and the ROI processed is the southern most part of the island. The phase that is present in these interferograms, $\phi$, has eight components:

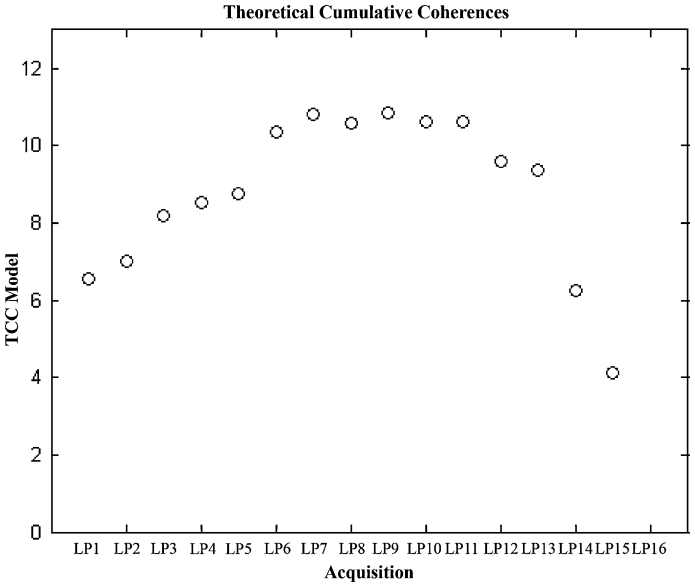


Figure 3
The theoretical cumulative coherences for each interferogram as a potential master image using the cumulative sum of the results from the TCC model.

$$\phi = \phi_{\text{geo}} + \phi_{\text{topo}} + \phi_{\text{atmos}} + \phi_{\text{offset}} + \phi_{\text{defo}} + \phi_{\text{dem\_error}} + \phi_{\text{noise}} + \phi_{\text{orbit\_error}} \quad (3)$$

The topographic phase, $\phi_{\text{topo}}$, can be removed during the generation of differential interferograms by subtracting the phase of the external DEM. The flat earth phase, $\phi_{\text{geo}}$, is removed using knowledge of the satellite positions. The slight difference in satellite position between two images ($\phi_{\text{orbit\_error}}$) produces a stereoscopic effect that can be removed by using using precise orbits calculated by TU Delft, Nederlands (SCHARROO and VISSER, 1998). Once these three components are removed, the typical components of a differential interferogram remain ($\phi_{\text{diff}}$),

$$\phi_{\text{diff}} = \phi_{\text{defo}} + \phi_{\text{atmos}} + \phi_{\text{offset}} + \phi_{\text{dem\_error}} + \phi_{\text{noise}}. \quad (4)$$

For $N$ images, there will be $N - 1$ differential interferograms. Therefore, there will be $N - 1$ phases, $\phi_i$, where $i = 1, 2, \ldots N - 1$. $\phi_{\text{defo}}$ accounts for the path length difference due to surface motion that occurs at different satellite passes, $\phi_{\text{atmos}}$ represents phase changes due to variations in the atmosphere, $\phi_{\text{offset}}$ takes into account that there will be an offset introduced during interferometric processing, $\phi_{\text{dem\_error}}$ represents the residual phase that is introduced by the difference in position between the DEM elevation and the scatterer, and $\phi_{\text{noise}}$ is the residual phase error due to noise. To accurately depict the deformation that is occurring on the island, the deformation component, $\phi_{\text{defo}}$, must be separated from the rest of the components.

## 4. Method 1: The Coherent Pixel Time Series Approach

High vegetation areas, characteristic of the North Atlantic subtropical islands with high topography, make differential radar interferometry more difficult because the vegetation causes the backscatter properties of the ground to change rapidly, causing the SAR pulses to reflect unequally over time resulting in a random component addition to the phase signal. Consequently, if an attempt is made to interpret decorrelated results produced by classical differential interferometry it could lead to a misinterpretation of the delayed differential phase. For this reason, we have applied a time series approach to the available SAR images that identifies the more reliable pixels based on a coherence threshold. The differential phase pattern of deformation is a relative measurement. Therefore, we can minimize the constant offset between interferograms to retrieve time continuous deformation information.

We have produced 15 independent interferograms using the *DORIS* software (KAMPES *et al*., 2003) implementing the two-pass differential interferometry method (MASSONNET and FEIGL, 1998). These interferograms have a 2:10 (range:azimuth) multi-look factor applied to them to gain coherence through spatial averaging. The topographic phase is removed from the raw interferograms using the SRTM3 Digital Elevation Model (DEM) and the stereoscopic effect is removed (derived from the perpendicular baseline) using precise orbits calculated by TU Delft, Nederlands (SCHARROO and VISSER, 1998). To remove the two-dimensional phase ambiguity (phase unwrapping), we used the average coherence ($\bar{\rho} = \frac{1}{N-1}\sum_{i=1}^{N-1} \rho_i$ with $i = 1, 2, \ldots, N-1$) on a pixel by pixel basis and substituted zeros for the complex values of the interferogram (phase/magnitude) associated with pixels that display low coherence (here, $\bar{\rho} < 0.35$) and then unwrapped the interferograms using the public software SNAPHU (CHEN, 2001). This selective rejection of pixels allows us to minimize the contribution of the low coherence areas (e.g. areas covering the sea and densely vegetated areas). Samples of unwrapped interferograms can be seen in Figure 4.

### 4.1. Removing Constant Offset

Differential interferograms produce a relative measurement, so we expect that the deformation data possess a constant offset for the whole interferogram that the unwrapping process cannot resolve. In order to estimate the time evolution of the deformation from the information contained in the differential interferograms, the constant offset must be removed from each one. It can be seen in Figure 5, that the coherence is low for most of the island. However, a large portion of the interferograms cover the sea which contains a large amount of random phase due to decorrelation. To deal with this decorrelation created by the water we want to refer all of the interferograms to an area known to be vertically stable.

To do this, a finite window taken about this stable region on the interferogram will be chosen. An average estimation of the phase value in a $n \times n$ finite window can be used to

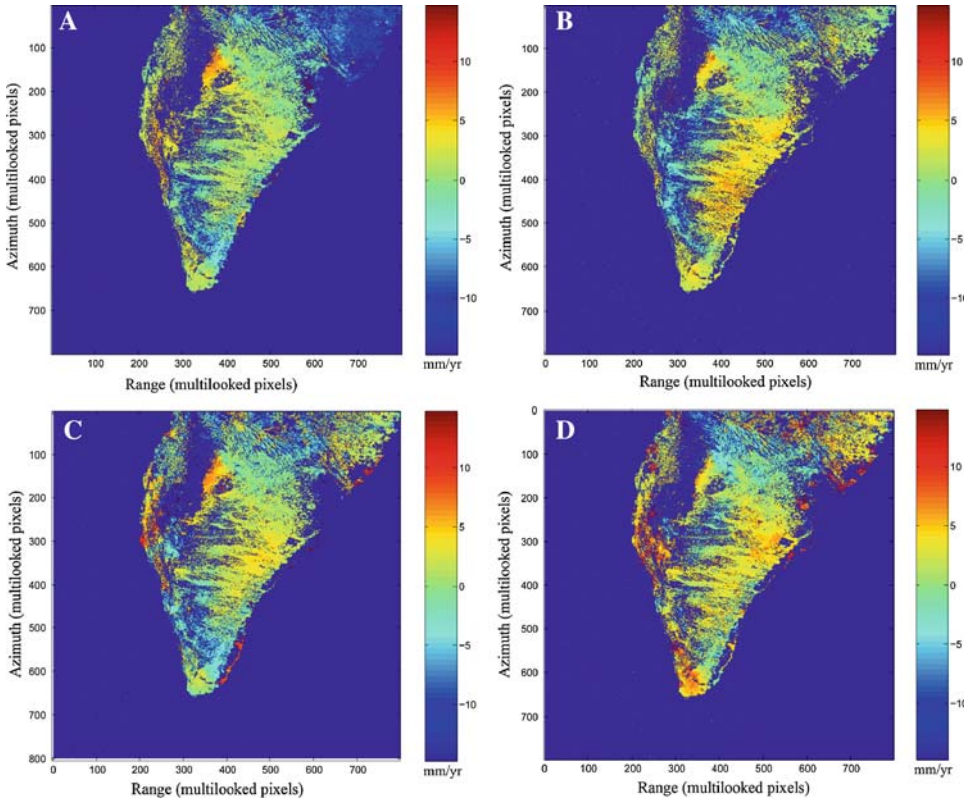


Figure 4

Unwrapped interferograms produced by the CPTS method with respect to the master image August 20, 1995. The dates for slave images used in each interferogram are as follows: A - May 29, 1992; B - September 9, 1996; C - October 14, 1996; D - June 21, 1999. For all images, the reference frame is in radar coordinates and deformation is presented in mm/yr.

approximate and remove the constant offset. Windows of different dimensions are considered to show the average offset values as a function of the window size, to determine how small a window can be and still be representative of the mean value that can be used to correct all of the interferograms. We test the mean value and standard deviations on the unwrapped phase inside 4 windows of variable size ($10 \times 10$, $20 \times 20$, $30 \times 30$, and $40 \times 40$) and find that the $20 \times 20$ window has almost the same mean phase value as the $30 \times 30$ and $40 \times 40$ windows (Fig. 6). From this analysis, we determined that a $20 \times 20$ pixel window is a good representation of the real mean-offset value.

### *4.2. Estimation of the Linear Velocity*

After removing the offset by addition or subtraction of the estimated phase value, we have an $N - 1$ time series. We transform these phase values to displacements in

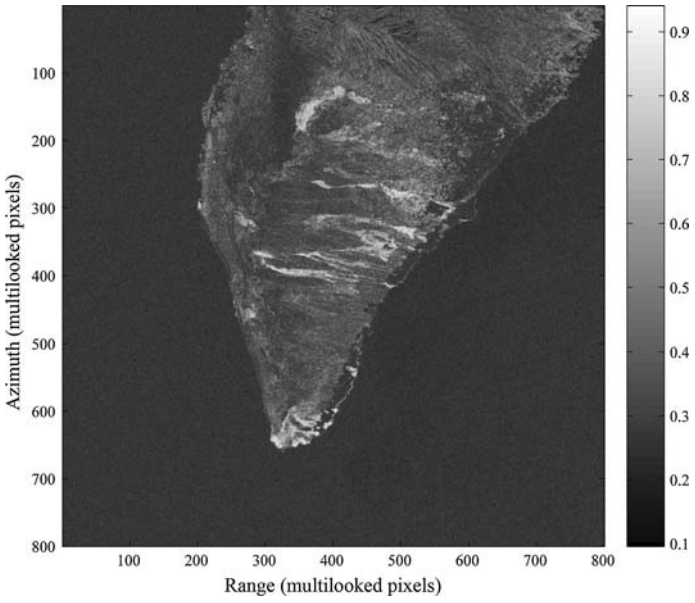


Figure 5
Average coherence for the 15 interferograms using August 20, 1995 as a master. The figure is represented in radar coordinates.

centimeters (using the knowledge of the carrier wavelength, for the ERS case $\lambda = 56.6$ mm). Using only 16 images, we are not able to distinguish the difference between nonlinear components due to atmospheric uncertainties and nonlinear components due to deformation. Consequently, we have only calculated an estimated map of the linear velocity of the displacement time series for the whole study area.

To estimate the linear velocity, we need to fit a line to our collection of displacement values. Let $t$ be the independent variable and let $y(t)$ denote a linear function of $t$ that we want to approximate. Assume there are $N - 1$ observations, i.e., values of $\hat{u}_{los}$ measured at specified values of $t$:

$$u_{losi} = y(t_i), \tag{5}$$

where $i = 1, 2, \ldots N - 1$. We want to model $y(t)$ using the equation,

$$y(t_i) = \beta_1 t + \beta_2. \tag{6}$$

To do this, we minimize the residuals using a least-squares method. We then estimate the linear velocity, by inverting to obtain the coefficients $\beta_j$ (where $j = 1, 2$) of the simple linear model. After fitting the linear model we use the norm of the error to reject points with high values that can be determined as a poor fit to the model. We construct the estimated map of linear velocity by simply multiplying the slope ($\beta_1$) of the model by 365, to obtain an estimate in mm/yr. Two masks are then applied to the maps. The first

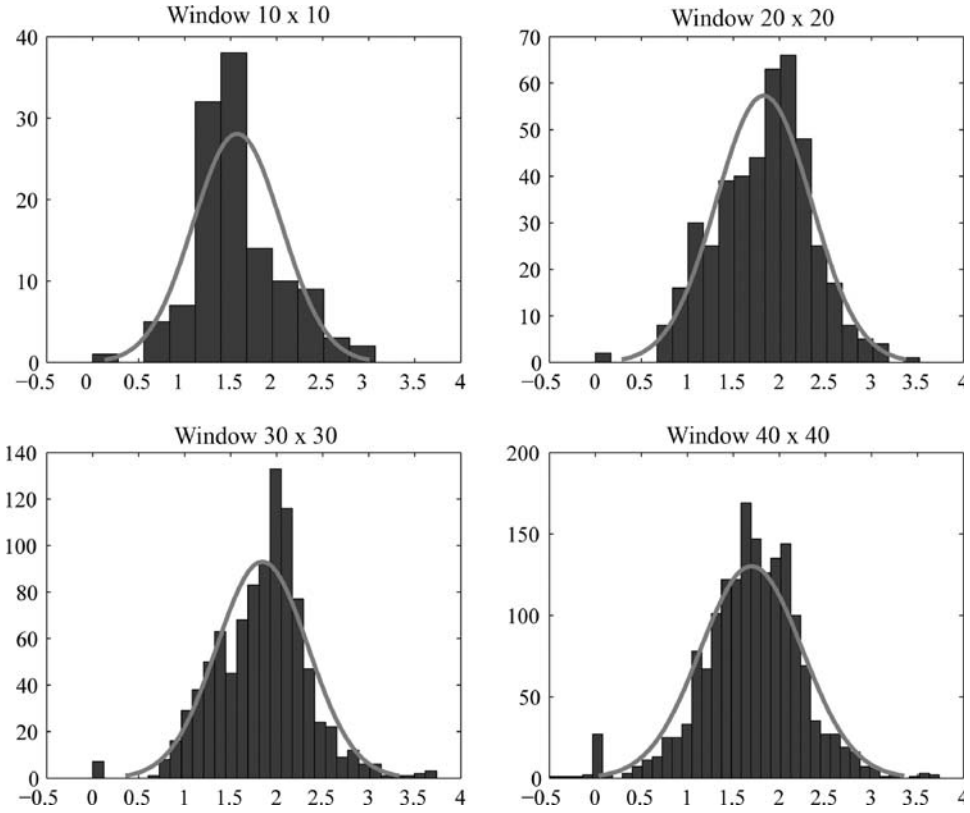


Figure 6
Histograms showing the constant offset estimation as a function of the window size. a) 10 × 10, b) 20 × 20, c) 30 × 30, and d) 40 × 40 (in pixels).

mask removes pixels below $\bar{\rho} = 0.35$ and the second mask removes the pixels that possess a high norm of errors (RMSError > 12 mm), under the assumption that these pixels do not contribute to the linear behavior with time. The results obtained here are presented in more detail in Section 6.

### 4.3. Error Estimation

As stated by KAMPES (2006), a model for the PS method is given by the equation,

$$\phi^k = \phi^k_{\text{topo}} + \phi^k_{\text{defo}} + \phi^k_{\text{atmo}} + \phi^k_{\text{noise}}. \tag{7}$$

Therefore, there are four separate terms that contribute independently to the reliability of the calculated differential phase ($\phi^k$) for each interferogram $k$.

The residual topographic component ($\phi^k_{\text{topo}}$) is present because the topographic phase that is removed from the interferogram is not exactly the same as the elevation read from the DEM, leaving a residual difference in elevation that will be added to the differential interferometric phase (RODRIGUEZ and MARTIN, 1992). To remove the topographic phase from the raw interferograms we have used the SRTM3 Digital Elevation Model (DEM), a global DEM released by NASA with a spatial resolution of 3 arcsec ($\approx$90 m) instead of estimating the errors as is done by FERRETTI *et al.* (2000; 2001) and HOOPER *et al.* (2004). This is done because the residual topographic phase is proportional to the perpendicular baseline and the SRTM3 DEM has relative errors of less than 7 m and absolute errors less than 16 m (FARR et al., 2007). Using the relation given by MASSONNET and FEIGL (1998), the cumulative sum of the perpendicular baseline for the La Palma images would be 1540 m (a cumulative error of 3.5 cm) over 27 years which translates to an error of approximately 1.8 mm/yr in linear velocity. This means we can have an error in the differential phase less than 1/2 of a half cycle in the *LOS* (MASSONNET and FEIGL, 1998). The contribution of this phase is also minimized by using multi-looked interferograms because in a multi-looked pixel, the phase value is the spatial average of many scatterers inside the pixel instead of a single point-like scatterer that could differ in altitude with respect to the reference DEM used to remove the topographic phase.

The deformation phase ($\phi^k_{\text{defo}}$) is computed using a linear model and estimated least-squares method that produces a relatively small error in the estimated slope between 0.5–1 mm/yr. Validation of this model was also done by performing a robust regression on the data. The difference in the results between these two methods was less than 0.5 mm/yr.

The atmospheric phase ($\phi^k_{\text{atmo}}$) is accounted for by applying an iterative robust regression to estimated the linear velocity from the interferometric phase time series. This acts as a time domain high pass filter, assigning lower weights to pixels that deviate significantly from the linear trend. Large residuals between the estimated model and the time series provide an additional parameter to assess the estimated linear velocity as they are used to mask pixels with high residual norms. Pixels with strong nonlinear behavior are most likely unwrapped poorly or contain significant atmospheric contributions.

The noise phase ($\phi^k_{\text{noise}}$) is either due to changes in the dielectric constant due to moisture content or to the sensor noise and is assumed to be a second-order effect that is purely random and therefore is not explicitly treated here.

By assessing the cumulative contribution of all of these errors to the differential phase, it is evident that linear velocities larger than 3–4 mm/yr identified by the CPTS approach are reliable.

## *5. Method 2: Coherent Target Analysis*

Coherent Target Modeling (CTM) was performed using commercial software developed by Atlantis Scientific Inc. version 3.1. CTM disregards the amplitude and uses

the phase stability of each pixel to determine its persistent scatterers. This is done by evaluating the temporal coherence (TC) of each pixel which is a measure of the stability of a scatterer over time. TC values tend to range between 0 and 1. More coherent pixels approach a TC value of 1 whereas incoherent pixels will tend towards a value of 0 (for further description see Equation (9)).

### 5.1. Deformation Model

The model begins by removing the atmospheric phase, $\phi_{\text{atm}}$, and the offset, $\phi_{\text{offset}}$. The phase is averaged over a 20 $\times$ 20 pixel window covering a stable region near the suspected deformation area and is used as an estimate of $\phi_{\text{atm}} + \phi_{\text{offset}}$. This estimate is then subtracted from the phase of the differential interferogram, $\phi_{\text{diff}}$, resulting in $\phi_{\text{atm\_corr}}$,

$$\phi_{\text{atm\_corr}} = \phi_{\text{defo}} + \phi_{\text{dem\_error}} + \phi_{\text{noise}}. \tag{8}$$

To separate out the vertical surface deformation from the phase, an iterative procedure searches a range of velocities ($\pm\ \phi_{\text{defo}}$) and a range of DEM errors, ($\pm\phi_{\text{dem\_error}}$) for each pixel. The process begins by calculating $\phi_i$ to $\phi_{N\text{-}1}$ by subtracting $\phi_{\text{defo}}$ and $\phi_{\text{dem\_error}}$ from $\phi_{\text{atm\_corr}}$. The temporal coherence for each pixel is then calculated,

$$TC = \frac{\sqrt{\left(\sum_{i=1}^{N-1}\cos(\phi_i)\right)^2 + \left(\sum_{i=1}^{N-1}\sin(\phi_i)\right)^2}}{N-1}. \tag{9}$$

The pair of $(\phi_{\text{defo}}, \phi_{\text{dem\_error}})$ that produces the highest temporal coherence value for each iteration is used as an estimate for the deformation, $\phi_{\text{defo}}$, and DEM error, $\phi_{\text{dem\_error}}$, respectively for each pixel.

To produce an enhanced image of the model, a second iteration of the procedure is performed using the temporal coherence threshold as a mask. At this point, the phase average used to remove the $\phi_{\text{atmos}} + \phi_{\text{offset}}$ is done over $\phi_{\text{diff}}$ using only those pixels that have a temporal coherence larger than the threshold. In each search window there must be a significant number of points with an appropriate value of temporal coherence for the average to be calculated, otherwise the average of the adjoining windows is used.

### 5.2. Specifics for La Palma

The processing for La Palma island was done using the Coherent Target Monitoring Panel software developed by Atlantis Scientific Inc. (Version 3.1). For coregistration, a minimum spatial overlap of 30% is defined and for both the range and azimuth, the minimum spectrum overlap is 50%. The search range for the deformation is $\pm$ 0.2 cycle/yr incremented in steps of 0.025 cycles/yr. The DEM error has a search range of $\pm$ 20.0 m with incremental steps of 1.0 m. The temporal coherence threshold used was 0.3.

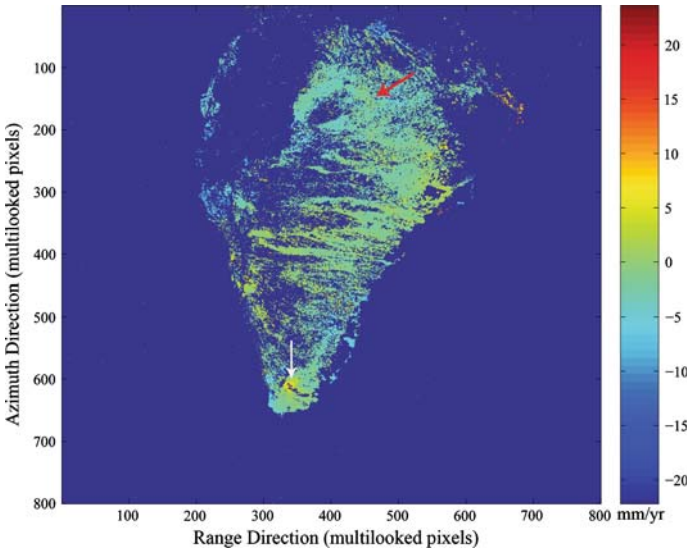


Figure 7

Map showing the estimation of the linear velocities for all of La Palma island determined by the CPTS approach. The deformation is presented in mm/yr using August 20, 1995 as a master image and is in radar coordinates. This image looks as if it has been flipped compared to Figure 10. This is due to the fact that this image is in radar coordinates and is therefore a mirror image of the geocoded image. Arrows represent the locations for the time series in Figures 12 and 13. The red arrow points to the stable location on the island used for constant offset removal and the white arrow points to the area of deformation around Teneguia volcano.

## *6. Results*

An important feature to notice in the CPTS application to the entire island (Fig. 7) is the absence of deformation in the northern section affecting the Cumbre Vieja volcano in its entirety. There has recently been discussion of a potential detachment surface beneath this ridge that has the possibility to create a landslide (Moss *et al.*, 1999; Day *et al.*, 1999). Differential InSAR tends to be more sensitive to vertical motion, but will still detect a projection of the horizontal motion in the LOS. Generally, if the motion is directed E-W then approximately 35% of the magnitude of the horizontal motion will be detected and similarly if the motion is in the N-S direction then the signal will be approximately 5% of the horizontal motion's magnitude. Therefore, it is unlikely that our processing would not detect at least a fraction of the horizontal motion's magnitude if it were present. Having said this, we also recognize the fact that this area could potentially be inactive during this time period and suggest that future studies should be conducted to monitor this region for activity.

In the CPTS approach we have neglected to estimate the atmospheric terms using filtering as in Ferretti *et al.* (2000; 2001) or Hooper *et al.* (2004). This is done by filtering phase values in a certain time window to remove the presence of outliers from

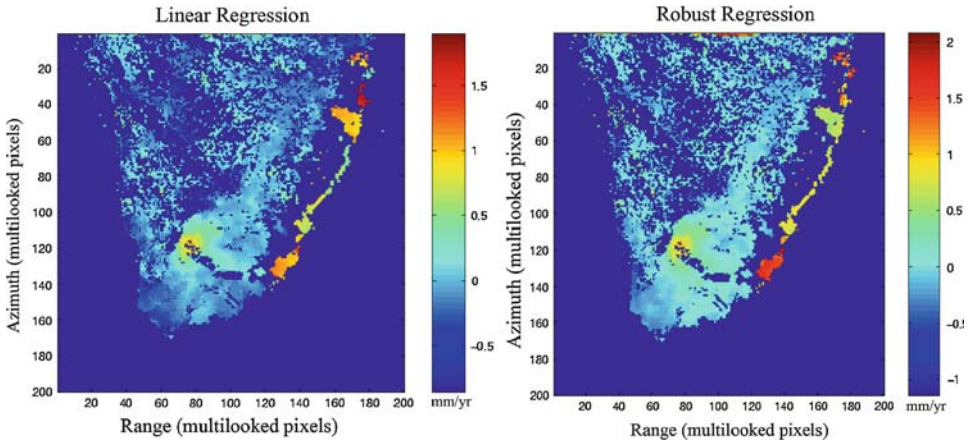


Figure 8

Left image is a map of the estimated linear velocity produced by the CPTS technique where deformation values have been fit using a linear regression. The image on the right represents estimated linear velocities produced by using a robust regression in the CPTS method. Both images are presented in radar coordinates and deformation is in mm/yr.

the actual deformation. To test if we were introducing a bias into the linear velocity by using a least-squares model (where all of the observations are weighted equally), we applied a robust regression to the same time series of phase values, and have found that the difference is negligible (Fig. 8). Therefore, we saw it as unnecessary to apply any time filtering using only 16 images.

In this method, it is the general trend of the time series being used to estimate the linear velocity that is important. When linear velocity is estimated in this way, the results show to be consistent with that of an independent method of stacking independent interferograms (Fig. 9).

Most importantly, the purpose of this paper is to present deformation that has previously not been identified by other InSAR techniques on La Palma island. There is a signal associated with this deformation in the southern part of the island (Figs. 10 and 11), where we observe a well-defined area of subsidence with a relatively high linear velocity. The time series associated with the deformation for the CPTS and CTM methods can be seen in Figure 12 and Figure 13, respectively. Comparing the results from the two techniques, there is a distinct, spatially consistent deforming area that defines a roughly circular shape with linear velocities of approximately $-4$ to $-8$ mm/year with a diameter on the order of 1 km centered on the Teneguia volcano (host of the last known eruption on La Palma in 1971). Classical interferometry methods have been unsuccessful at identifying any deformation on La Palma. Therefore, this is the first time that this deformation has been detected on La Palma using InSAR methods.

The signal is more easily identified using the results from the CPTS technique which could be due to the small number of SAR images used. It is suggested that a minimum of 30 images should be used for the best results with CTM (Atlantis Scientific Inc., 2004)

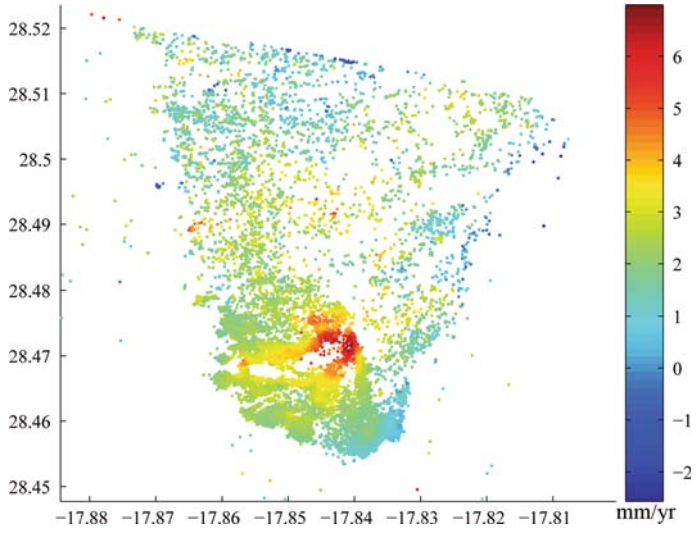


Figure 9

Stack of 5 independent interferograms with long time separation and small perpendicular baselines. Interferograms used are: 19920529-19950924 (1213 days; − 29.1 m); 19920807-19960108 (1249 days; 30.8 m); 19930723-20000726 (2509 days; 72.1 m); 19950611-19961014 (491 days; 21.8 m); and 19950821-19990621 (1400 days; − 14.7 m) where bracketed values are (time difference; perpendicular baseline). Linear velocity values are expressed in mm/yr.

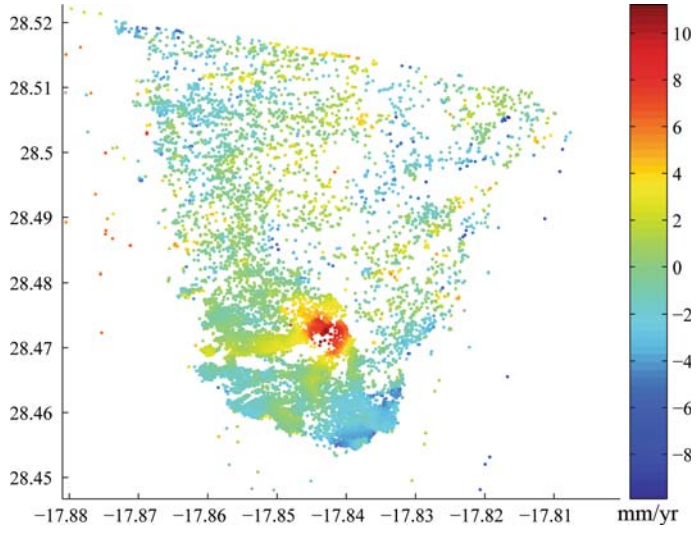


Figure 10

Map showing the estimation of the linear velocities calculated using the CPTS approach for the southern part of La Palma island focusing on the region of deformation detected in Figure 7. The deformation is presented in mm/year using August 20, 1995 as a master image.

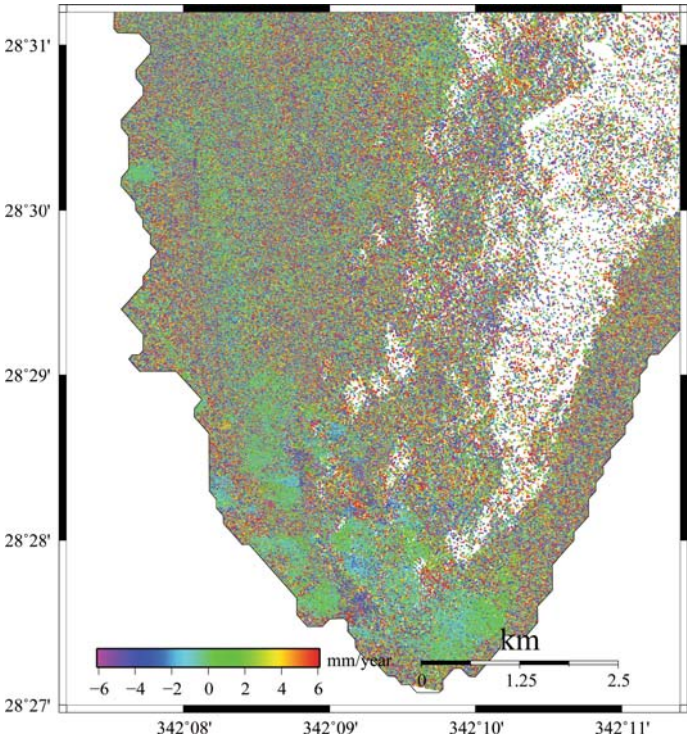


Figure 11
Map showing the estimation of the linear velocities calculated using the Coherent Target Modeling method for the southern part of La Palma island focusing on the region of deformation detected in Figure 7 using August 20, 1995 as a master image.

but due to a lack of images we were forced to process the data with only 15 images. Regardless of the noise due to this issue, a circular pattern comparable to that seen in the CPTS approach is still identifiable in the image.

## 7. *Discussion*

Water vapor is a major source of error when measuring ground deformation using differential interferometry (HANSSEN, 2001). In general, water molecules will absorb and reflect radar signals differently depending on their phase state (liquid, solid or gaseous) (SKOLNIK, 1990). Water vapor in the gaseous phase delays radar waves more than liquid drops or ice crystals, resulting in phase delays proportional to the number of clouds in the region. Due to the high topography in the Canary Islands we can distinguish three different layers in the lower troposphere: (1) A fresh and moist layer located below 700 m, (2) a thermal inversion layer between 700 m and 1500 m that prevents convection

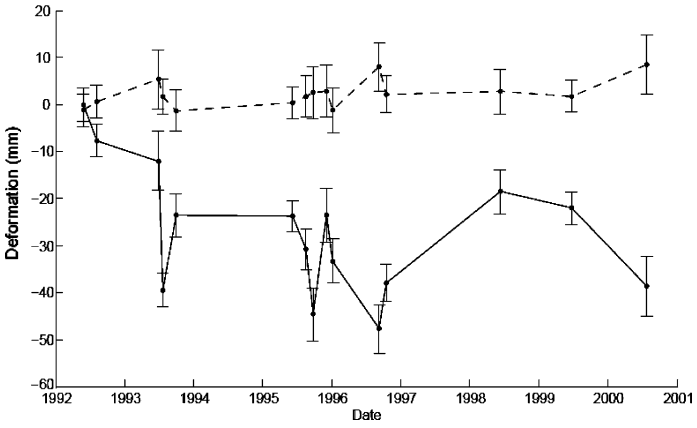


Figure 12

Time series produced for 2 separate pixels using the CPTS technique. Data connected by a solid line correspond to a pixel in the deforming Teneguia region represented by a white arrow in Figure 7 and data connected by a dotted line correspond to a pixel located in the stable area used to remove the constant offset represented by a red arrow in Figure 7. Errorbars are estimated as the standard deviation in the 20 × 20 pixel window and assigned for each date. Negative values indicate an increase in LOS.

of the water vapor, and (3) a higher dry layer above 1500 m (García Herrera *et al.*, 2001). Therefore, when interpreting differential interferograms for the whole island, vertical stratification and its presence over time should be taken into account. However, the Fuencaliente area where we have detected deformation is a smaller region located at a lower elevation and due to its size, we believe that it is too small to contain prevalent atmospheric signals, either from turbulent behavior of the water vapor or from a horizontal pattern that reflects the vertical stratification of the lower troposphere. Also, the effects of tropospheric water vapor on the velocity estimates are likely to be quite small as tropospheric water vapor is generally uncorrelated on the timescales of InSAR image acquisition repeat time. We can therefore, assume that the signal that is detected is due strictly to ground surface motion.

Possible sources for the deformation detected include gravitational loading from previously erupted material, withdrawal of magma from a shallow magma chamber, ground water removal, or a thermal anomaly. If the deformation were due to gravitational loading from erupted material, the signal should be similar to that of the size of Teneguia's cone. However, Teneguia's cone is approximately 500 m and the deformation detected here extends approximately 1 km horizontally. Likewise, the withdrawal of magma from a shallow magma chamber is usually simulated using deep point sources that generate vertical deformations that extend radially with a magnitude of approximately half the depth to the point source. Therefore, the withdrawal of magma from the chamber would be associated with a much larger signal than we are seeing here. Groundwater removal can be discredited as a source because there is no known aquifer in this

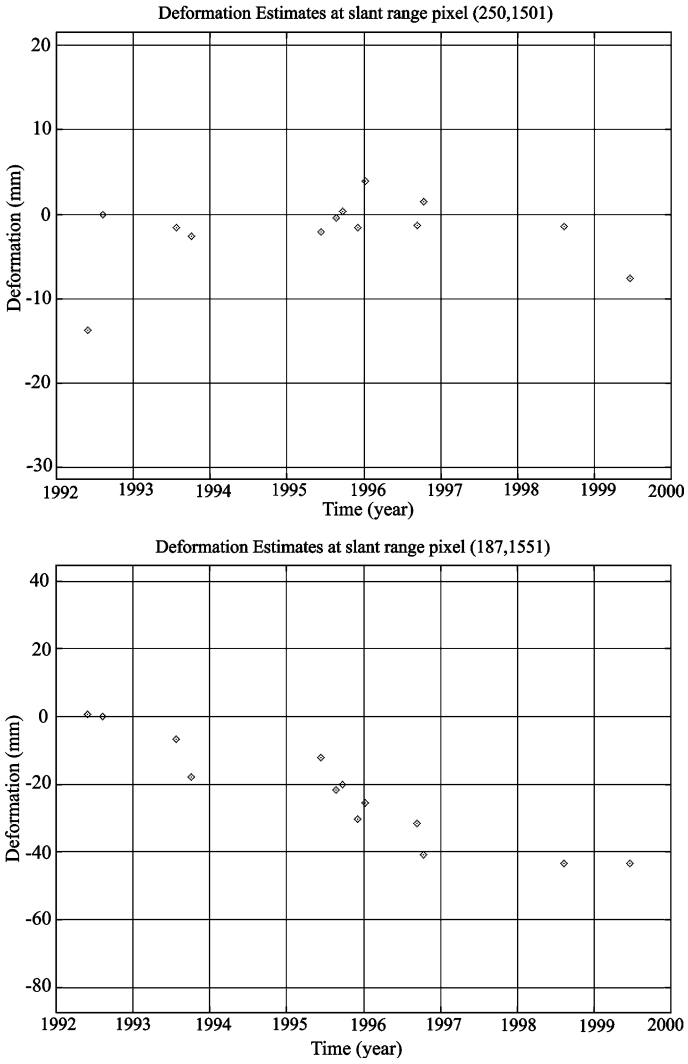


Figure 13

Figure 13A is the time series produced for a pixel in the stable region used for atmospheric corrections in the CTM approach taken from the area identified by the red arrow in Figure 7. Figure 13B is the time series produced for a pixel in the deforming area around Teneguia volcano determined by the CTM approach, represented by a white arrow in Figure 7.

region. However, La Palma island is known to have thermal anomalies with subsurface temperatures that exceed 300° Celsius (ABAD FERNÁNDEZ and SÁNCHEZ GUZMÁN 1985) and contains a recognized shallow depth Hot Dry Rock geothermal system (HDRS) in its southern part in the Fuencaliente region. In addition to this, to the southwest of the Teneguia volcano, the existence of a hot spring well at the base of the cliff has been

verified. This evidence leads us to conclude that a thermal source is the most likely possibility for this deformation.

## *8. Conclusions*

Large advances have been made in the last decade in the study of radar interferometry as a geodetic tool. The technique has proven useful in volcanic areas to detect rapid displacements cause by shallow intrusions, as well as slow long-standing inflation-deflation processes in deep magmatic reservoirs. Despite these advances, the monitoring of natural terrains with dense vegetation can still be difficult and troublesome.

We studied an eight year period from 1992 to 2000 using data from the ERS-1 and ERS-2 satellites to create maps of the surface ground deformation on the densely vegetated island of La Palma. By applying two different InSAR phase analysis techniques (CPTS technique and CTM) we have detected a spatially consistent deforming area that defines a roughly circular shape with linear velocities of approximately $-4$ to $-8$ mm/year covering an area of $\sim 1$ km in diameter centered on the Teneguia volcano. We have also noticed that there is an absence of deformation (at the precision level of this study) in the northern region previously linked to a detachment surface beneath the Cumbre Vieja volcano. However, there is a possibility of inactivity in this area during the time period studied and suggest that future studies be done to continue monitoring this region for activity.

Classical interferometry methods have been unable to detect any deformation on La Palma because of difficulties due to the atmospheric interference, terrain and dense vegetation on the island. The methods presented here are limited by the small set of SAR images available and by the fact that the CPTS approach produces only estimates of the mean velocities. However, they have been successful over previous conventional differential InSAR methods because they have a higher sensitivity and a fine spatial resolution, allowing us to detect deformation at La Palma island for the first time using InSAR processing. Future research will involve acquiring more SAR images of the island and modeling the thermal anomalies causing deformation. These techniques can also be applied for the semi-continuous monitoring of large scale landslides and to obtain a better knowledge of the thermal ground deformation in the Fuencaliente area.

## *Acknowledgements*

This research is part of the GEOMOD project funded by the Spanish Ministry of Education and Science (MEC) under contract (CGL2005-05500-C02). Data was kindly provided by ESA, in the frame of the Category-1 Project (ID:2679) and the DECIDE Volcano projects. Research by KFT was funded by an NSERC Discovery Grant. The work by PP was funded by a Province of Ontario Early Researcher Award. This research has also been partially supported by the Spanish Research Project PCI2006-A7-0660.

## References


Abad Fernández, J. and Sánchez Guzmán, J. (1985), *Geothermal energy in the Spanish energy plan: Present status of the most advanced projects*, Geothermics *14*, 379–384.

Ancoechea, E., Hernán, F., Cendrero, A., Cantagrel, J. M., Fúster, J. M., Ibarrola, E., and Coello, J. (1994), *Constructive and destructive episodes in the building of a young Oceanic Island, La Palma, Canary Islands, and the genesis of the Caldera de Taburiente*, J. Volcanol. Geotherm. Res. *60*, 243–262.

Anguita, F. and Hernán, F. (1975), *A propagating fracture model versus a hotspot origin for the Canary Islands*, Earth Planet. Sci. Lett. *27*, 1119.

Anguita, F. and Hernán, F. (2000), *The Canary Islands origin: A unifying model*, J. Volcanol. Geotherm. Res. *103*, 1–26.

Araña, V. and Ortíz, R., *The Canary Islands: Tectonics, magmatism and geodynamic framework*. In *Magmatism in Extensional Structural Settings: The Phanerozoic African Plate* (eds. Kampunzu, A. B. and Lubala, R. T.) (Springer-Verlag, Berlin, 1991), pp 209–249.

Atlantis Scientific Inc., *EV-InSAR Version 3.1 User's Guide* (Atlantis Scientific Inc., Nepean, Ontario, 2004).

Banda, E., Dañobeitia, J. J., Suriñach, E., and Ansorge, J. (1981), *Features of crustal structure under the Canary Islands*, Earth Planet. Sci. Lett. *55*, 11–24.

Bravo, T. (1964), *Estudio Geológico y Petrográfico de la Isla de La Gomera*, Estudios Geológicos *20*, 93–108.

Carracedo, J. C., Day, S., Guillou, H., Rodríguez, E., Canas, J. A., and Pérez, F. J. (1998), *Hotspot volcanism close to a passive continental margin*, Geological Magazine *135*, 591–604.

Carracedo, J. C., Rodríguez-Badiola, E., Guillou, H., Nuez, J. D. L., and Pérez-Torrado, F. J. (2001), *Geology and volcanology of La Palma and El Hierro, Western Canaries*, Estudios Geológicos *57*, 175–273.

Chen, C. W. (2001), *Statistical-Cost Network-Flow Approaches to Two-Dimensional Phase Unwrapping for Radar Interferometry*, Ph.D. Thesis, Stanford University.

Dañobeitia, J. J. and Canales, J. P. (2000), *Magmatic underplating in the Canary Archipelago*, J. Volcanol. Geotherm. Res. *103*, 27–41.

Day, S., Carracedo, J. C., Guillou, H., and Gravestock, P. (1999), *Recent structural evolution of the Cumbre Vieja Volcano La Palma, Canary Islands: Volcanic rift zone reconfiguration as a precursor to volcano flank instability?*, J. Volcanol. Geotherm. Res. *94*, 135–167.

De La Nuez, J. (1984), *El Complejo Intrusivo Subvolcánico de la Caldera de Taburiente* (La Palma, Canarias), Ph.D. Thesis, Universidad Complutense de Madrid.

Farr, T. G., Rosen, P. A., Caro, E., Crippen, R., Duren, R., Hensley, S., Kobrick, M., Paller, M., Rodriguez, E., Roth, L., Seal, D., Shaffer, S., Shimada, J., Werner, J. U. M., Oskin, M., Burbank, D., and Alsdorf, D. (2007), *The Shuttle Radar Topography Mission*, Rev. Geophys. *45*, doi:10.1029/2005RG000183.

Fernández, C., De la Nuez, J., Casillas, R., and García-Navarro, E. (2002), *Stress fields associated with the growth of a large shield volcano (La Palma, Canary Islands)*, Tectonics *21*, 41–57.

Ferretti, A., Prati, C., and Rocca, F. (2000), *Nonlinear subsidence rate estimation using permanent scatterers in differential SAR interferometry*, IEEE Trans. Geosci. Remote Sens. *38*, 2202–2212.

Ferretti, A., Prati, C., and Rocca, F. (2001), *Permanent scatterers in SAR interferometry*, IEEE Trans. Geosci. Remote Sens. *39*, 8–20.

Fúster, J. M., Araña, V., Brändle, J. L., Navarro, J. M., Alonso, V., and Aparicio, A., *Geología y Volcanología de Las Islas Canarias: Tenerife* (Instituto Lucas Mallada, CSIC, 1968).

García Herrera, R., Gallego Puyol, D., Hernández Martín, E., Gimeno Presa, L., and Ribera Rodríguez, P. (2001), *Influence of the North Atlantic oscillation on the Canary Islands precipitation*, J. Climate *14*, 3889–3903.

Guillou, H., Carracedo, J. C., and Day, S. (1998), *Dating of the upper Pleistocene-Holocene volcanic activity of La Palma using the unspiked K-Ar technique*, J. Volcanol. Geotherm. Res. *86*, 137–149.

Hanssen, R. F., *Radar Interferometry: Data Interpretation and Error Analysis* (Kluwer Academic Publishers, Dordrecht, 2001).

Hildenbrand, A., Gillot, P.-Y., Soler, V., and Lahitte, P. (2003), *Evidence for a persistent uplifting of La Palma* (*Canary Islands*), inferred from morphological and radiometric data, Earth Planet. Sci. Lett. *210*, 277–289.

Hooper, A. (2006), *Persistent Scatterer Radar Interferometry for Crustal Deformation Studies and Modeling of Volcanic Deformation*, Ph.D. Thesis, Stanford University.

HOOPER, A., ZEBKER, H., SEGALL, P., and KAMPES, B. (2004), *A new method For measuring deformation on volcanoes and other non-urban areas using InSAR persistent scatterers*, Geophys. Res. Lett. *31*, L23611, doi:10.1029/2004GL021737.

KAMPES, B. M., *Radar Interferometry: Persistent Scatterer Technique*, Remote Sensing and Digital Image Processing Series (Springer Ed., Dortrecht, The Netherlands, 2006).

KAMPES, B. M., HANSSEN, R. F., and PERSKI, Z., *Radar Interferometry with Public Domain Tools*. In Proc. FRINGE 2003 Workshop, Frascati, Italy (2003).

KLÜGEL, A., HANSTEEN, T. H., and GALIPP, K. (2005), *Magma storage and underplating beneath Cumbre Vieja Volcano, La Palma (Canary Islands)*, Earth Planet. Sci. Lett. *236*, 211–226.

MASSONNET, D. and FEIGL, K. L. (1998), *Radar interferometry and its application to changes in the Earth's surface*, Rev. Geophys. *36*, 441–500.

MASSONNET, D. and SIGMUNDSSON, F., *Remote sensing of volcano deformation by radar interferometry from Various Satellites*. In *Remote Sensing of Active Volcanism* (eds Mouginis-Mark, P. J., Crisp, J. A., and Fink, J. H.), Geophysical Monographs *116* (Am. Geophys. Union, Washington, DC, 2000), pp 207–221.

MIRANDA, N., ROSICH, B., SANTELLA, C., and GRION, M., *Review of the impact of ERS-2 piloting modes on the SAR Doppler stability. In Proc. 2004 Envisat & ERS Symp., 6-10 September 2004*, Salzburg, Austria (ESA SP-572, April 2005) (2004).

MOSS, J., MCGUIRE, W., and PAGE, D. (1999), *Ground deformation monitoring of a potential landslide at La Palma, Canary Islands*, J. Volcanol. Geotherm. Res. *94*, 251–265.

NAVARRO, J. M. and COELLO, J. J., *Mapa Geológico del Parque Nacional de la Caldera de Taburiente* (ICONA. Ministerio de Agricultura, Pesca y Alimentación, 1993).

PÉREZ, N. M., WAKITA, H., NAKAI, S., SANO, Y., and WILLIAMS, S. N. (1994), $^{3}$He/$^{4}$He *isotopic ratios in volcanic hydrothermal discharges from the Canary Islands, Spain: Implications on the origin of the volcanic activity*, Mineralogical Magazine *58A*, 709–710.

RODRIGUEZ, E. and MARTIN, J. M. (1992), *Theory and design of interferometric synthetic aperture radars*, IEE Proceedings-F *139*, 147–159.

ROMERO, C., *Actividad Volcánica Histórica en Las Islas Canarias*. In *Curso Internacional de Volcanología y Geofísica Volcánica* (Excmo. Cabildo Insular de Lanzarote, Lanzarote, Islas Canarias, 2000), pp 115–128.

SCHARROO, R. and VISSER, P. (1998), *Precise orbit determination and gravity field improvement for the ERS satellites*, J. Geophys. Res. *103*, 8113–8127.

SKOLNIK, M., *Radar Handbook* (McGraw-Hill Inc., 1990).

ZEBKER, H. A. and VILLASENOR, J. (1992), *Decorrelation in Interferometric Radar Echoes*, IEEE Transactions on Geoscience and Remote Sensing *30*, 950–959.

(Received May 14, 2007, revised May 4, 2008, accepted May 6, 2008)